Journal of Materials Research and Technology 30 (2024) 4137–4146

Contents lists available at ScienceDirect

Journal of Materials Research and Technology

journal homepage: www.elsevier.com/locate/jmrt

Numerical analysis of Al_2O_3 and TiO_2 growth and oxygen dissolution in a metal substrate during the isothermal oxidation of an α-Ti alloy at 973 K

Tomonori Kitashima [a,b,*], Takanobu Hiroto [c], Makoto Watanabe [a]

[a] Research Center for Structural Materials, National Institute for Materials Science, 1-2-1 Sengen, Tsukuba, Ibaraki, 305-0047, Japan
[b] Department of Materials, Kyushu University, 744 Motooka Nishi-ku, Fukuoka, 819-0395 Japan
[c] Research Network and Facility Services Division, National Institute for Materials Science, 1-2-1 Sengen, Tsukuba, Ibaraki, 305-0047, Japan

ARTICLE INFO

Handling Editor: SN Monteiro

Keywords:
Oxidation
Titanium alloy
Oxide growth
Oxygen dissolution
Kinetic modeling

ABSTRACT

Oxide growth of Al_2O_3 and TiO_2 as well as O dissolution during the oxidation of an α-Ti alloy at 973 K were simulated using the finite volume method coupled with the calculation of phase diagrams (CALPHAD) method. The results indicated that the addition of 11.02 at.% Al to a Ti–O system resulted in the formation of an 18-nm-thick Al_2O_3 layer, which decelerated TiO_2 growth and O dissolution in the substrate. An increase in the O concentration at the oxide–metal interface was also inhibited by Al_2O_3 formation. A thin Al-depletion zone was formed at the oxide–metal interface. Furthermore, Al_2O_3 formation was restricted by the low concentration and diffusivity of Al in the substrate.

1. Introduction

Ti alloys have traditionally been used as components in jet engines due to their high strength-to-density ratio and corrosion resistance. Their performance in high-temperature components, such as those in high-pressure compressors, is critical because the temperature capability of these components influences the final jet engine performance. Therefore, Ti alloys have been developed with improved high-temperature properties. Recently, novel near-α alloys containing approximately 6 wt% Al have been designed for applications at 923–973 K [1,2].

Oxidation resistance is an important property for high-temperature applications. During the oxidation of Ti and its alloys in air, oxide scales grow on the metal surface and O dissolves from the surface into the metal substrate. This O dissolution occurs due to the high solubility limit of O in α-Ti [3], which increases the hardness of the metal surface in the O dissolution zone [4]. Such surface property changes due to oxide growth and O dissolution in Ti alloys increase the susceptibility of the alloys to crack nucleation and propagation under creep, cyclic loading, and/or cyclic temperature changes [5–7]. For example, the O dissolution zone leads to embrittlement and rapid crack nucleation during cyclic loading, resulting in a shorter fatigue lifetime [6,7]. Therefore, understanding the underlying mechanism of oxidation in Ti alloys is important for enhancing their mechanical properties in high-temperature environments.

For the oxidation of pure Ti, Stringer [8] reported that the overall parabolic rate constant can be described as the sum of the parabolic rate constants for the growth of the oxide scale and O dissolution layers. This relationship has been subsequently demonstrated in pure Ti between approximately 873 and 973 K [9,10]. Similarly, the parabolic rate constant has been previously studied for O dissolution in α- and α–β-Ti alloys [4,11–15]. The O dissolution depth has been demonstrated to be affected by the alloy composition [14,16]. However, the activation energies for O dissolution in α- and α–β-Ti alloys were similar between 833 and 923 K [13]. Therefore, the role of different elements in O dissolution during the oxidation of Ti alloys, which is also affected by the proportion of constitutional phases in the substrate, remains unclear.

The oxidation behavior of Ti alloys depends on the alloy composition [17]. Al is a critical element whose addition enhances solid-solution strengthening and promotes the formation of protective Al_2O_3 at the metal surface during high-temperature oxidation. Oxide scale formation in Al-added α- and α–β-Ti alloys has been extensively studied for Ti–6Al–4V (Ti-64) [14,15,18], Ti–6Al–2Sn–4Zr–2Mo (Ti-6242) [11–14,19], IMI-834 [20], and other Ti alloys [4,21,22]. During the oxidation of Al-containing alloys, inner titania (TiO_2) and outer α-alumina (Al_2O_3) form and grow on the metal surface. When the oxide scales grow to a certain extent, cracks are generated between them and the substrate. These cracks grow further and detach the oxide scales from the

* Corresponding author.
E-mail address: KITASHIMA.Tomonori@nims.go.jp (T. Kitashima).

https://doi.org/10.1016/j.jmrt.2024.04.164
Received 25 December 2023; Received in revised form 14 April 2024; Accepted 18 April 2024
Available online 20 April 2024

substrate, resulting in the formation of new TiO_2 and Al_2O_3 oxides on the metal substrate [18]. This repeating process causes the formation of alternating TiO_2 and Al_2O_3 layers on the alloy substrate, with the number of alternating layers increasing with increasing temperature and exposure time.

Compared with TiO_2, Al_2O_3 exhibits a lower solid-state diffusion rate for cations and O through the oxide [23,24]. During oxidation, Al_2O_3 formed on the surface acts as a diffusion barrier, slowing down oxide growth and O penetration into the substrate through the oxide scales. The resulting decrease in O dissolution in a metal was previously demonstrated by microhardness measurements in the metal zone [16]. Meanwhile, a first-principles study demonstrated that an increase in the Al content increases the O binding energy at Ti (0001) surfaces and that Al substitution in a metal facilitates O migration into the subsurface [25]. However, although the roles of Al in oxide growth and O dissolution during the oxidation of Al-added Ti alloys have been reported, their relationship and underlying mechanisms have not been adequately clarified, partly because the high rate of O dissolution in the substrate during oxidation complicates their behavior. In addition, Al_2O_3 formed in oxide scales is extremely thin; consequently, few studies have reported the growth behavior and thickness of Al_2O_3 due to the difficulty in distinguishing the boundaries between TiO_2 and Al_2O_3. To the best of the authors' knowledge, no systematic simulations or quantitative discussions of the growth behavior of TiO_2 and Al_2O_3 have been conducted thus far.

The oxidation resistance at 973 K is crucial for evaluating the applicability of new high-temperature Ti alloys. At this temperature, oxidation follows a parabolic rate law in binary Ti–Al alloys, Ti-64, and Ti-6242 [11,15,26]. However, this parabolic kinetic transitioned to a linear rate law after long time exposures such as 150 h for Ti-64 [15] and 200 h for Ti-6242 [11] to 973 K, which can accelerate surface property degradation. Therefore, it is important to elucidate the effect of Al addition on oxide growth behavior and elemental concentration evolution in the substrate during the diffusive oxidation reaction at this temperature. In this study, the growth of Al_2O_3 and TiO_2 and the temporal changes in the O dissolution depth during oxidation in a Ti–Al–O system were evaluated at 973 K for 50 h using numerical simulations coupled with the calculation of phase diagrams (CALPHAD) method. In addition, the temporal changes in the elemental concentration profiles of the substrate during oxidation were demonstrated at 973 K. The overall weight gain and temporal changes in the total oxide thickness were measured experimentally, and the results were incorporated into the iterative calculations in the simulation. The effect of Al_2O_3 formation on TiO_2 growth and O dissolution in the metal substrate during the oxidation of the Ti–Al–O system was examined by comparing the oxidation behavior of the system with that of Ti–O.

2. Experimental section

Ingots (1.1 kg) of pure Ti and Ti–6.5Al were produced using the cold crucible levitation melting method. Both ingots were double-melted to enhance their compositional uniformity. The atomic percentage (at.%) compositions of these materials were Ti–0.17O and Ti–11.02Al–0.13O, measured using inert gas fusion–infrared absorption for O and wet chemical analysis for Al. Plates measuring 15 mm in thickness, 20 mm in width, and 40 mm in length were machined from the ingots and heat-treated in Ar-filled quartz capsules at 1073 K for 4 h, followed by air cooling. Cylindrical specimens (10 mm in diameter and 4 mm in height) were machined from the inside of the heat-treated plates for use in the oxidation tests. The surfaces of the specimens were polished using 1200-grit SiC paper and subjected to ultrasonic cleaning in acetone.

Isothermal oxidation tests were conducted under ambient atmospheric conditions. Samples of pure Ti and Ti–6.5Al in alumina crucibles were oxidized together in a furnace at 973 K for 10, 20, 45, 70, 90, and 140 h before removal and air cooling. The mass change of each sample was determined using a microbalance with an accuracy of 0.0001 g. The constituent oxide phases were identified by X-ray diffraction (XRD) analysis using a SmartLab diffractometer (Rigaku) with Cu Kα radiation (λ = 1.5418 Å) generated at 45 kV and 200 mA. The overall oxide thickness of the oxidized specimens was measured using a JEOL JSM 7001F field emission gun scanning electron microscope (FEG-SEM) after metallographic polishing using conventional techniques. Chemical single-line analysis was performed using an energy-dispersive X-ray spectrometer attached to the FEG-SEM equipment.

3. Modeling

The oxidation of Ti–0.17O and Ti–11.02Al–0.13O at 973 K in air was modeled. The oxide scales formed on the substrates were assumed to grow inward at the oxide–metal interface [27]. In addition, rutile-TiO_2 and/or α-Al_2O_3 were assumed to form on the substrate in the current Ti–Al–O system. The concentration equations for the substrate were solved using the boundary conditions of the elemental concentrations at the oxide–metal interface (Fig. 1), which were iteratively determined by comparing the overall weight gain obtained from the measured and simulated results. The formation of TiO_2 and Al_2O_3 oxide scales was determined by examining the O partial pressure at which the substrate and oxide coexisted. The O partial pressure was calculated using the CALPHAD method based on the elemental concentrations at the substrate oxide–metal interface. Additional details of the modeling and calculation procedure are presented in the following subsections.

3.1. Governing equations

The atomic percentage distributions of Al and O in the substrate were obtained by solving one-dimensional diffusion equations using the Eulerian expression, as follows:

$$\frac{\partial C_i}{\partial t}=\frac{\partial}{\partial x}\left(D_i\frac{\partial C_i}{\partial x}\right)+V_I\frac{\partial C_i}{\partial x}, \tag{1}$$

where i represents Al and O; C_i (at.%) denotes the concentration of element i; x (m) is the coordinate in the spatial direction normal to the oxide–metal interface; V_I (m/s) is the migration velocity of the oxide–metal interface; and D_i (m^2/s) is the diffusion coefficient of element i in Ti, determined as follows [9,28]:

$$D_{Al}=\left(6.6\times10^{-3}\right)\exp\{-329,000/(RT)\}, \tag{2}$$

$$D_O=\left(5.0\times10^{-3}\right)\exp\{-241,344/(RT)\}, \tag{3}$$

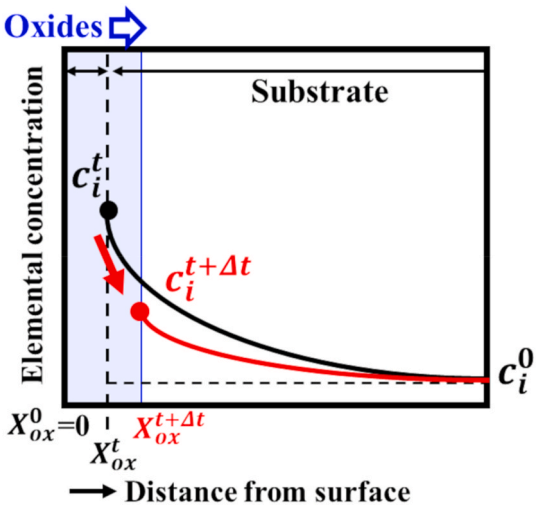

Fig. 1. Schematic of the temporal changes in the elemental concentration profile of an α-Ti alloy substrate accompanied with oxide growth.

where R is the gas constant (8.314 J/K/mol), and T (K) is the temperature. Al diffuses substitutionally while O diffuses interstitially in a hexagonal close-packed substrate structure. The nondiagonal components of the diffusion equations were not considered because few diffusion coefficients were available and the contributions of the nondiagonal components to diffusion were relatively small. The effect of oxide–metal interface migration on diffusion was considered, as expressed by the last term in Eq. (1). The interface migration velocity was obtained by differentiating the approximate equation for the temporal changes in oxide thickness, as described in Section 4. The initial and boundary conditions are described in Section 3.4. The number of grids was set to 30,000 [10]. The implicit finite volume method was employed to discretize the time-dependent equations, which were solved using the tridiagonal matrix algorithm. The diffusion term in Eq. (1) was discretized using a second-order central difference scheme, and the time step was 0.1 s.

3.2. Thermodynamic calculation of oxide formation

This study assumes that the following oxidation reactions for pure Ti and Ti–6.5Al occur at 973 K:

$$Ti + O_2 = TiO_2, \tag{4}$$

$$\frac{4}{3}Al + O_2 = \frac{2}{3}Al_2O_3. \tag{5}$$

The O partial pressures at which the substrate and oxide coexist at the oxide–metal interface can be described as follows:

$$P_{TiO_2} = \frac{a_{TiO_2}}{a_{Ti}} exp\left(\frac{\Delta G^0_{TiO_2}}{RT}\right), \tag{6}$$

$$P_{Al_2O_3} = \frac{a^{2/3}_{Al_2O_3}}{a^{4/3}_{Al}} exp\left(\frac{\frac{2}{3} \bullet \Delta G^0_{Al_2O_3}}{RT}\right). \tag{7}$$

The standard free energies of formation of the oxides, $\Delta G^0_{TiO_2}$ and $\Delta G^0_{Al_2O_3}$, were obtained from thermochemical data [29]. Assuming that mutual dissolution of the oxides did not occur, the activities of TiO_2 and Al_2O_3 (a_{TiO_2} and $a_{Al_2O_3}$) were 1. The activities of Ti and Al in the substrate were obtained from their chemical potentials at the oxide–metal interface using the following relation:

$$a_i = \exp\left(\frac{\mu_i - \mu^0_i}{RT}\right), \tag{8}$$

where i represents Ti and Al; μ_{Ti} and μ_{Al} are expressed as follows:

$$\mu_{Ti} = G^{hcp}_m - \sum_{i=Al,O} \frac{\partial G^{hcp}_m}{\partial c_i} c_i, \tag{9}$$

$$\mu_{Al} = \mu_{Ti} + \frac{\partial G^{hcp}_m}{\partial c_{Al}}. \tag{10}$$

G^{hcp}_m, $\frac{\partial G^{hcp}_m}{\partial c_{Al}}$, $\frac{\partial G^{hcp}_m}{\partial c_O}$, μ^0_{Ti}, and μ^0_{Al} were calculated using the thermodynamic parameters of the ternary Ti–Al–O system [30]. The procedure to determine the oxides formed on the substrate is described in Section 3.4.

3.3. Weight gain due to oxide growth and O dissolution

Inner TiO_2 and outer Al_2O_3 layers were formed on the surface during the oxidation of Al-added Ti alloys. However, the boundary between TiO_2 and Al_2O_3 was difficult to determine. In a previous study, Valdés-Saucedo et al. [31] demonstrated the formation of a layer consisting of a mixture of rutile TiO_2 and nonprotective Al_2O_3 clusters at the initial stage of oxidation of Ti–4Al–2.5V at 1123, 1173, and 1273 K, despite the dependence of the surface morphology and oxide structure on the oxidation temperature. In addition, Nijdam et al. [32] demonstrated that the formation of a layered structure of oxides during oxidation successfully described the oxidation behavior of a Ni–Al–Cr alloy. Similarly, in the present study, the formation of a continuous layer of each oxide (TiO_2 and Al_2O_3) was assumed due to the one-dimensional nature of the simulation, which can be regarded to represent the small diffusion barrier effect of the thin Al_2O_3 layer. The total oxide thickness at time $t + \Delta t$ can be described as the sum of the two oxide thicknesses:

$$X_{ox} = X_{Al_2O_3} + X_{TiO_2}. \tag{11}$$

The elemental consumption due to the growth of each oxide is equivalent to the change in the concentration of each element in the substrate:

$$\frac{m_{Al}}{V_{Al_2O_3}} X_{Al_2O_3} = \int_0^L C^{m,0}_{Al} dx - \int_{X^{t+\Delta t}_{ox}}^L C^{m,t+\Delta t}_{Al} dx, \tag{12}$$

$$\frac{m_{Ti}}{V_{TiO_2}} X_{TiO_2} = \int_0^L C^{m,0}_{Ti} dx - \int_{X^{t+\Delta t}_{ox}}^L C^{m,t+\Delta t}_{Ti} dx, \tag{13}$$

where L represents the distance from the initial surface of the substrate, m_{Al} and m_{Ti} denote the number of moles of Al and Ti per mole of oxide, and $V_{Al_2O_3}$ and V_{TiO_2} denote the molar volumes of the oxides (25.6 and 18.8 cm^3/mol for Al_2O_3 and TiO_2, respectively). The molar concentrations of Al and Ti at time $t + \Delta t$, $C^{m,t+\Delta t}_{Al}$, and $C^{m,t+\Delta t}_{Ti}$ were obtained using $C^{t+\Delta t}_{Al}\rho^{t+\Delta t}_m / M^{t+\Delta t}$ and $C^{t+\Delta t}_{Ti}\rho^{t+\Delta t}_m / M^{t+\Delta t}$, respectively, by assuming that the local density, $\rho^{t+\Delta t}_m$, did not affect the concentration in Eq. (1). $M^{t+\Delta t}$ denotes the molar mass, calculated as follows:

$$M^{t+\Delta t} = \sum_{i=Al,O,Ti} A_i C^{t+\Delta t}_i, \tag{14}$$

where A_i denotes the atomic weight of element i. $\rho^{t+\Delta t}_m$ is calculated as follows:

$$\frac{1}{\rho^{t+\Delta t}_m} = \sum_{i=Al,O,Ti} \frac{A_i C^{t+\Delta t}_i / M^{t+\Delta t}}{\rho_i}, \tag{15}$$

where ρ_i denotes the density of element i.

The weight gain per unit area at time $t + \Delta t$ due to oxide growth was calculated by multiplying the oxide thickness, oxide density, and O weight fraction in each oxide:

$$W_{Al_2O_3} = X_{Al_2O_3} \bullet \rho_{Al_2O_3} \bullet W^O_{f,Al_2O_3}, \tag{16}$$

$$W_{TiO_2} = X_{TiO_2} \bullet \rho_{TiO_2} \bullet W^O_{f,TiO_2}, \tag{17}$$

where $\rho_{Al_2O_3}$ and ρ_{TiO_2} represent the densities of TiO_2 and Al_2O_3, respectively, and W^O_{f,Al_2O_3} and W^O_{f,TiO_2} represent the O fractions of each mole of oxide (0.40 and 0.47, respectively). During the growth of oxide scales and O dissolution, the elemental concentrations at the oxide–metal interface change based on Eqs. (12) and (13).

The weight gain at time $t + \Delta t$ due to O dissolution was obtained from the following relation:

$$W_O = \int_{X^{t+\Delta t}_{ox}}^L \rho^{t+\Delta t}_m \bullet W^{t+\Delta t}_{f,O} dx - \int_0^L \rho^0_m \bullet W^0_{f,O} dx, \tag{18}$$

where $W^{t+\Delta t}_{f,O}$ is the local weight fraction of O at time $t + \Delta t$, as calculated from $A_O C^{t+\Delta t}_O / M^{t+\Delta t}$.

3.4. Initial/boundary conditions and calculation procedure

The calculation field L, representing the distance from the initial surface of the substrate, was set to 80 μm. This distance was sufficiently large to calculate the elemental concentration distribution and compare the oxide thicknesses and O dissolution depths. The initial elemental concentrations ($t = 0$) were homogeneous, indicating that they were equivalent to their bulk concentrations. Specifically, $C_O = 0.17$ at.% for pure Ti, and $C_{Al} = 11.02$ at.% and $C_O = 0.13$ at.% for Ti–6.5Al, as described in Section 2. After the initiation of oxidation ($t > 0$), the boundary condition for the inner concentrations at $x = L$ was set as follows:

$$\left.\frac{\partial C_i}{\partial x}\right|_{x=L} = 0. \tag{19}$$

The calculation procedure was as follows: (i) At time $t + \Delta t$, the approximate weight gain, Eq. (20), was calculated. The migration velocity of the oxide–metal interface was determined by differentiating the approximate Eq. (21)–(23) for the oxide thickness; (ii) Eq. (1) was then iteratively solved using the implicit finite volume method until the residuals were below 0.001; (iii) after the calculation of Eq. (1) converged, the weight gains due to oxide growth and O dissolution were calculated using Eq. (16)–(18); (iv) the difference between the values obtained by the approximate Eq. (20) and the sum of Eq. (16)–(18) was calculated; and (v) when the difference was ≥ 0.01%, C_i at the oxide–metal interface was changed according to the oxides formed on the substrate, as described below, and the calculation reverted to step (ii). When the difference was <0.01%, the calculation reverted to step (i) after C_i at time $t + \Delta t$ was set as the value at time t. When the convergent C_O at the oxide–metal interface was higher than 32.9 at.% after iteration, C_O was fixed to that value, whereas C_{Al} at the oxide–metal interface was set to 0.01 at.% when C_{Al} was <0.01 at.%. Notably, for the first iteration at time $t + \Delta t$, C_i was initially changed at step (v) due to the difference between the measured weight gain at $t + \Delta t$ and the simulated weight gain obtained using C_i at t.

During oxidation in the Ti–Al–O system, the following formation and growth of TiO_2 and/or Al_2O_3 on the metal surface were considered: (i) Al_2O_3 only, (ii) Al_2O_3 and TiO_2, and (iii) TiO_2 only. In this study, the oxides formed on the substrate were determined by comparing the O partial pressures expressed by Eqs. (6) and (7) for TiO_2 and Al_2O_3, respectively. The chemical potentials in Eqs. (9) and (10) were calculated from the elemental concentrations at the oxide–metal interface. In a previous study, Nijdam et al. [33] simulated the formation of Al_2O_3, Cr_2O_3, and NiO during the oxidation of a Ni–Al–Cr alloy at 1373 K in one dimension by assuming local equilibrium at the oxide–metal interface. The calculated temporal evolution of the elemental concentrations at the oxide–metal interface was in good agreement with the experimental results.

The standard free energy of formation of Al_2O_3 is lower than that of TiO_2 at 973 K; therefore, the iterative calculation of C_i at the oxide–metal interface was started by assuming that only Al_2O_3 formed (i.e., case (i)). If C_i in case (i) did not eliminate the difference between the weight-gain values obtained using the approximate Eq. (20) and the sum of Eq. (16)–(18), then C_i was determined from the composition field for case (ii). Fig. 2(a) presents the O partial pressures for TiO_2 and Al_2O_3 at 10 at.% O in the Ti–Al–O system at 973 K, which were obtained from Eqs. (6) and (7). TiO_2 was stable at Al concentrations below approximately 2 at.%, whereas Al_2O_3 was more stable when the Al concentration exceeded 2 at.%. An intersection was observed when both TiO_2 and Al_2O_3 were in equilibrium with the substrate (point A in Fig. 2(a)). With the variation in the O content of Ti–11.02Al–0.13O at 973 K, an equilibrium line for the Ti–Al–O alloy for TiO_2 and Al_2O_3 was observed (Fig. 2(b)). Notably, the Al concentration required to form Al_2O_3 gradually decreased to approximately zero at 32.9 at.% O. This indicates that Al_2O_3 forms even at low Al concentrations until an O content of 32.9 at.% is reached, which is close to the solubility limit of O in α-Ti. It was assumed that only TiO_2 was formed when C_i at the oxide–metal interface was equivalent to C_i in the TiO_2 field in Fig. 2(b) (case (iii)).

4. Results and discussion

Fig. 3 displays backscattered-electron images of oxide scales for pure Ti and Ti–6.5Al after 90 and 140 h of oxidation at 973 K. The results demonstrate that oxide scales grew on the metal surfaces, with negligible crack formation observed at the metal–oxide interface after 90 h. However, after 140 h, substantial cracks were observed in the Ti–6.5Al substrate near the oxide scales (Fig. 3(d)). The high concentration of Al, which serves as a solid-solution strengthening element, in Ti–6.5Al may have increased the brittleness of the surface due to O dissolution. However, it is unclear whether the cracks formed during oxidation or specimen preparation. In addition, cracks have been previously reported to grow between the metal and internal TiO_2 layers during oxidation [18]. Notably, the oxide scale thickness on pure Ti was consistently larger than that on Ti–6.5Al for the oxidation times studied.

Subsequently, XRD analysis was performed on the surfaces of the samples after 140 h of oxidation (Fig. 4(a)). The main constituent oxide was identified as rutile TiO_2 in both pure Ti and Ti–6.5Al. Reflections of α-Ti were also detected in both matrix materials due to the penetration of the X-rays through the oxide scales. A TiN peak was detected for pure Ti. This indicates the occurrence of nitride formation and nitrogen dissolution on the metal surfaces, which has been previously reported during the high-temperature oxidation of Ti alloys [22,34]. A small

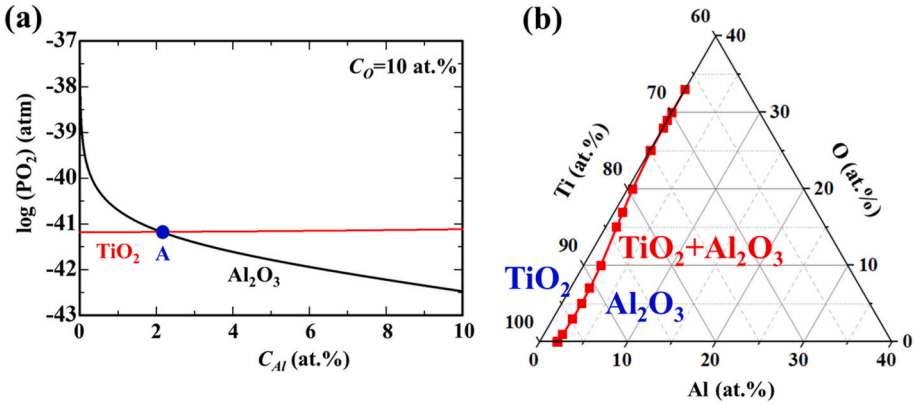

Fig. 2. (a) O partial pressures at which the substrate and TiO_2 and/or Al_2O_3 coexist during the oxidation of α-Ti with 10 at.% O at 973 K, as obtained by the CALPHAD method using thermodynamic parameters [30]. Point A is the intersection point of the two curves. (b) Diagram illustrating the relative atomic concentrations of thermodynamically equilibrated oxides in the Ti–Al–O system at 973 K.

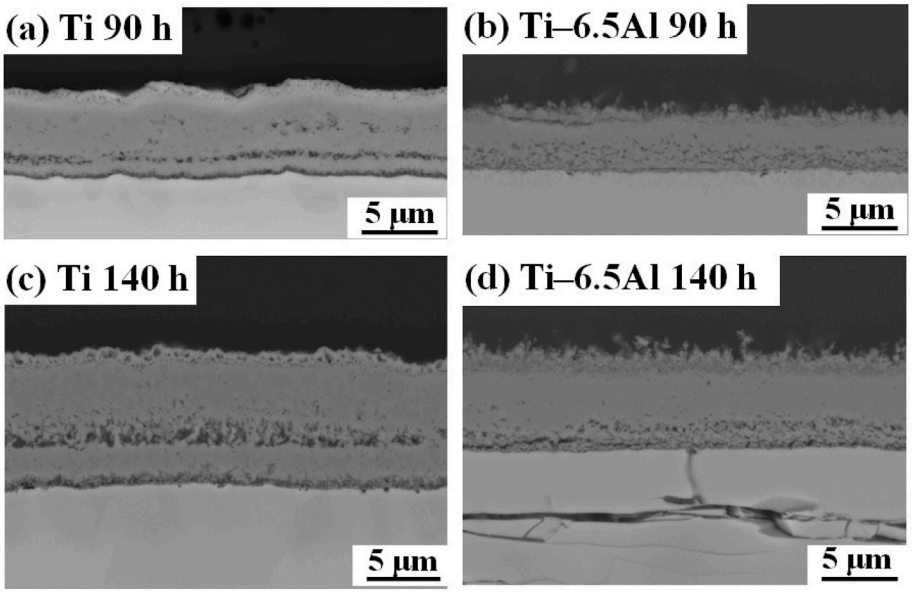

Fig. 3. Backscattered-electron images of oxide scales after oxidation at 973 K: (a) pure Ti and (b) Ti–6.5Al after 90 h; (c) pure Ti and (d) Ti–6.5Al after 140 h.

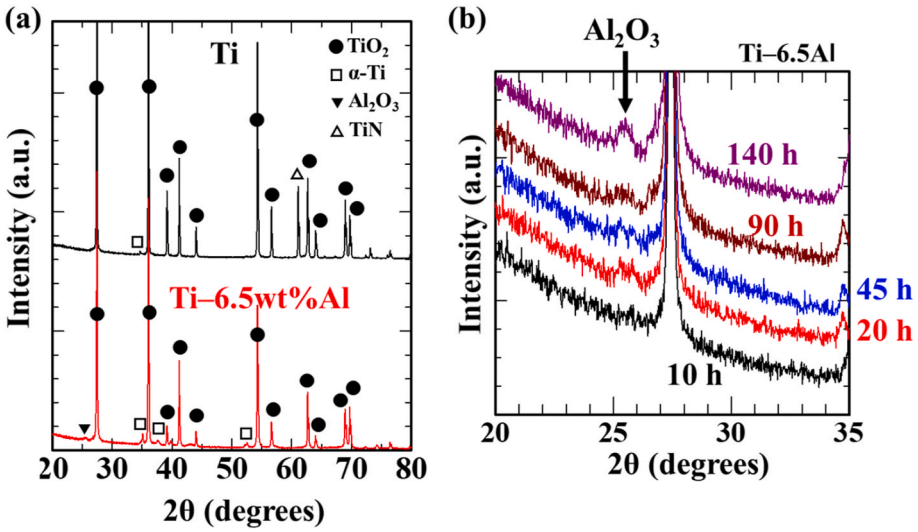

Fig. 4. (a) XRD patterns of pure Ti and Ti–6.5Al after oxidation at 973 K for 140 h. (b) XRD patterns of Ti–6.5Al between 20° and 35° after oxidation for 10, 20, 45, 90, and 140 h at 973 K.

α-Al_2O_3 peak was detected in the Ti–6.5Al pattern after 20, 45, 90, and 140 h of oxidation (Fig. 4(b)). However, the indistinct nature of this peak makes it difficult to quantitatively determine the Al_2O_3 thickness.

The Al, O, and Ti concentration line profiles for the oxide layers and Ti–6.5Al substrate after 10, 20, and 45 h of oxidation are presented in Fig. 5(a), (b), and (c), respectively. The profiles demonstrate that the oxides were composed of internal TiO_2 and external Al_2O_3-rich layers; however, the boundary between each layer was not clearly defined. Porosity was observed in TiO_2 near the oxide–metal interface, as illustrated in Fig. 5. The inner porous layer grew as the oxidation time increased from 10 to 45 h. Chou et al. [35] demonstrated the growth of a two-layer TiO_2 during the oxidation of pure Ti. The outer dense layer of TiO_2 initially grew at a faster rate and slowed down, while the inner porous scale of TiO_2 exhibited a constant growth rate [35]. In addition, it has been suggested that the porous layer of TiO_2 allows rapid O penetration into the oxide–metal interface [36,37]. However, the porosity formation mechanism remains unclear and requires further investigation. The total oxide thickness was measured by scanning electron microscopy after each oxidation time. The results clearly indicated that the oxide scale thickness increased as the oxidation time increased.

Fig. 6 shows XRD patterns obtained from the sample surfaces of pure Ti and Ti–6.5Al after oxidation for 10, 20, and 45 h at 973 K, where the low-intensity peaks are magnified. XRD patterns obtained after 140 h of oxidation is also presented in Fig. 6 for comparing the results obtained between the early stages and after longer exposure. In this study, the oxide mainly comprised rutile-TiO_2 for pure Ti and Ti–6.5Al. This result is consistent with numerous previous studies on the oxidation of pure Ti and Ti alloys, although there is a possibility of the formation of different oxides, such as TiO, Ti_2O_3, and Ti_3O_5, during Ti oxidation from the viewpoint of thermodynamics and comparison with the sequent oxide formation in Fe oxidation [18,38]. Some studies have demonstrated the minor formations of Magnéli phases, such as Ti_2O_3 and TiO, in oxide scales during oxidation in Ti and its alloys [18,26,39]. In addition, it has been suggested that the order–disorder transformation, resulting in Ti_6O, may occur in the substrate near the metal–oxide interface because

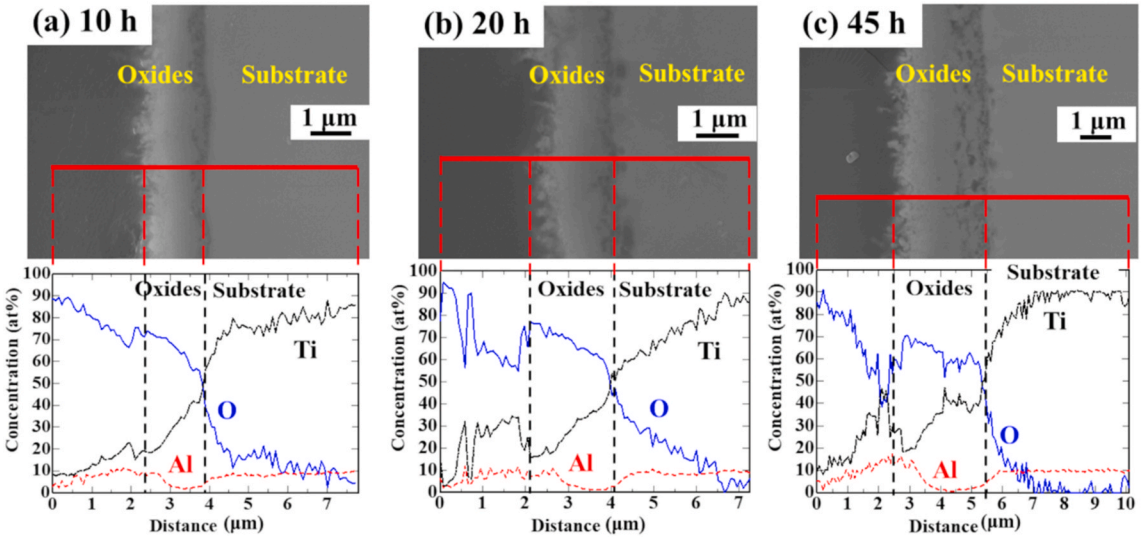

Fig. 5. EDS concentration profiles of Ti, Al, and O obtained for the oxides and Ti–6.5Al substrate after (a) 10, (b) 20, and (c) 45 h of oxidation at 973 K.

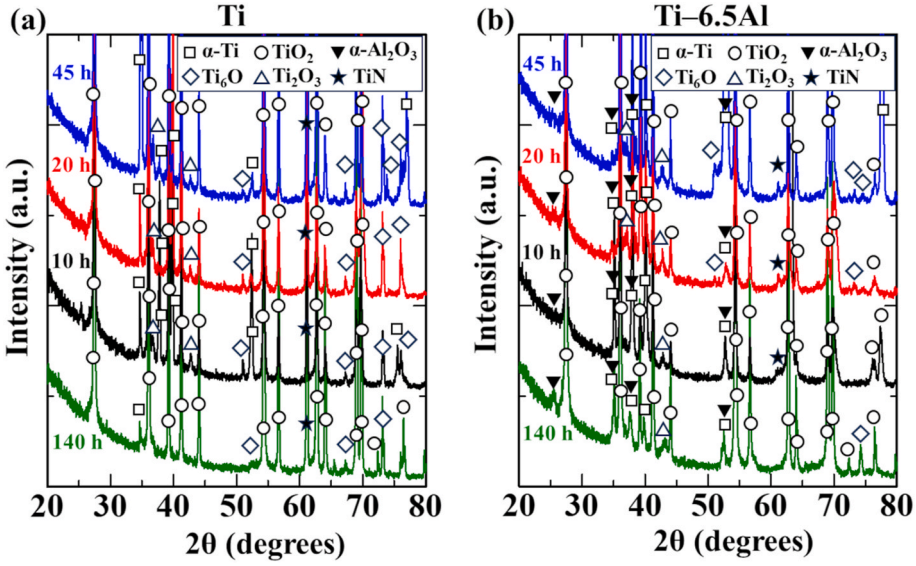

Fig. 6. Magnified-minor-phase peaks in the XRD patterns of (a) pure Ti and (b) Ti–6.5Al after oxidation for 10, 20, 45, and 140 h at 973 K.

of the O solid solution [9,36]. In this study, the low-intensity peaks of minor phases obscured the effect of Al addition on minor-phase formation and the growth behavior of minor phases with time. However, the fraction of minor phases might be less than a few percent, which was also suggested by a previous study [38].

Different types of metastable Al_2O_3 phases, e.g., γ, δ, and θ, were formed during oxidation in Al-containing alloys [26,39–42] and transformed to the stable α-Al_2O_3 phase according to the routes of metastable Al_2O_3 transforming into α-Al_2O_3 [41,42]. This Al_2O_3 phase transformation occurs earlier with increasing the oxidation temperature. Although there is a high possibility of the formation of metastable Al_2O_3 phases in this study, only low-intensity peaks of α-Al_2O_3 were observed (Fig. 6(b)), whereas other types of Al_2O_3 were not detected in the XRD patterns. This is probably because peaks corresponding to the metastable Al_2O_3 phases were very weak and overlapped with other strong intensity peaks. There has been no report on the dependency of the Al_2O_3 phase transformation on time, temperature and Al composition in α- and α–β-Ti alloys. Therefore, in the simulation of this study, α-Al_2O_3 phase formation was assumed to occur during oxidation in Ti–6.5Al.

Fig. 7(a) and (b) display the measured weight gain and oxide thickness, respectively, in pure Ti and Ti–6.5Al as functions of time. The measured weight gain and oxide thickness were fitted to power-law models [11,15,18] (as indicated by the solid lines in Fig. 7):

$$\left(\frac{\Delta W}{A}\right)^n = k_n t, \tag{20}$$

$$(X_{ox})^m = k_m t, \tag{21}$$

where $\Delta W/A$ represents the weight gain per unit surface area, X_{ox} represents the oxide layer thickness, n and m are the reaction indices, k_n and k_m are the rate constants, and t is the time. For Ti and Ti–6.5Al, n was determined to be 1.49 and 1.67, respectively, while k_n was determined to be 6.03×10^{-12} and 5.61×10^{-13} mg cm^{-1} s^{-1}, respectively. Based on the reaction indices, the oxidation of both pure Ti and Ti–6.5Al followed linear–parabolic kinetics for the first 90 h of oxidation at 973 K. Meanwhile, for the oxide thicknesses of pure Ti, m and k_m were 1.52 and 3.70×10^{-5} μm/s, respectively. Notably, the approximate equation for the oxide thickness of Ti–6.5Al up to 10 h was fitted to a proportional relationship to avoid a strong initial increase in thickness, which was not

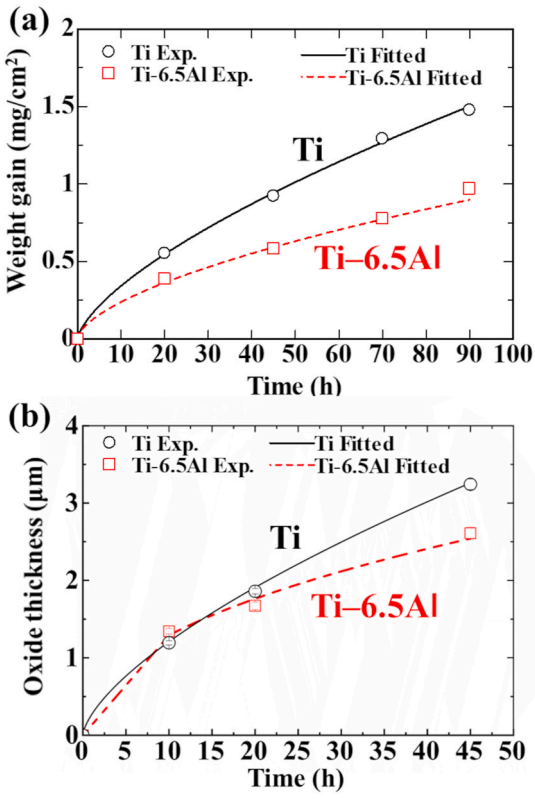

Fig. 7. (a) Measured and fitted weight gain of pure Ti and Ti–6.5Al after 90 h of oxidation at 973 K. (b) Measured and fitted temporal changes in the oxide thickness of pure Ti and Ti–6.5Al after 45 h of oxidation at 973 K.

experimentally observed in this study.

The equations obtained for the oxide thickness of Ti–6.5Al are therefore expressed as:

$$X_{ox} = k_{lin} t \text{ for } t < t_1, \tag{22}$$

$$(X_{ox})^m = k_m t \text{ for } t \geq t_1, \tag{23}$$

where $t_1 = 10$ h (36,000 s); $k_{lin} = X_{ox}|_{t=t_1}/t_1$; $X_{ox}|_{t=t_1}$ represents the oxide thickness obtained using Eq. (23) at t_1; and m and k_m are 2.22 and 4.90 $\times 10^{-5}$ μm/s, respectively. These approximate equations were employed in the simulations. As illustrated in Fig. 7, the experimental data were in relatively good agreement with the approximated lines for both weight gain and oxide thickness for both samples. The rates of weight gain and oxide thickness increase in Ti–6.5Al were lower than those in pure Ti; however, the oxide thickness was similar in pure Ti and Ti–6.5Al after 10 h of oxidation, as illustrated in Fig. 7(b). This may be due to the insufficient barrier effect of Al_2O_3 formation on oxide growth at short oxidation times.

In the simulations, the elemental concentrations at the metal–oxide interface were iteratively determined until the simulated total weight gain corresponded to that obtained by the approximate equation indicated by the solid line in Fig. 7(a). Therefore, the simulated total weight gains were in good agreement with the measured values for pure Ti and Ti–6.5Al, as illustrated in Fig. 8(a) and (b). The simulated weight gain due to TiO_2 growth in pure Ti (59.8%) was larger than that due to O dissolution (40.2%). In a previous study, Unnam et al. [9] reported weight gains of 1.208 and 0.554 mg/cm^2, respectively, for oxide growth and O dissolution in pure Ti with an initial O concentration of 0.14 wt% after 92.2 h at 977 K. By comparison, the values obtained in this study for oxide growth and O dissolution were 0.904 and 0.619 mg/cm^2, respectively, after 92 h at 973 K. The results of the present study indicate a smaller contribution from TiO_2 growth than that in the previous study.

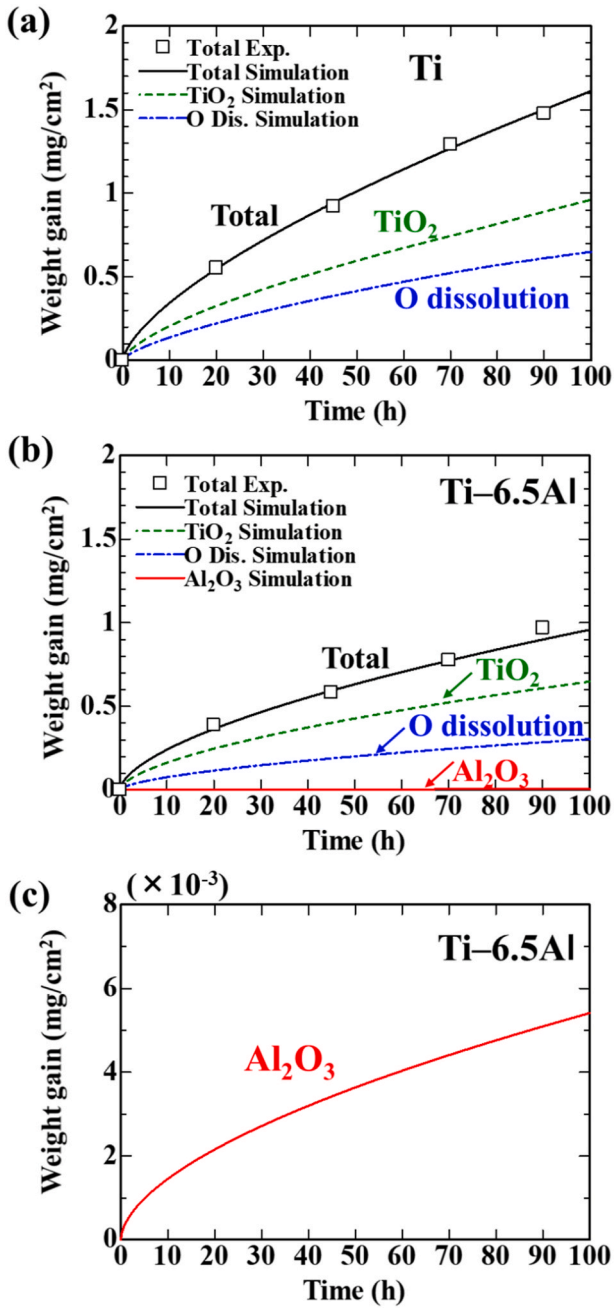

Fig. 8. Measured and simulated total weight gain and simulated contributions of TiO_2/Al_2O_3 growth and O dissolution to the weight gain of (a) pure Ti and (b) Ti–6.5Al. (c) Magnified simulated weight gain due to Al_2O_3 growth in Ti–6.5Al, as depicted in (b).

For Ti–6.5Al, the total weight gain was smaller than that for pure Ti, with smaller weight gains due to both TiO_2 growth and O dissolution. The weight gain due to Al_2O_3 growth was smaller than that due to both TiO_2 growth and O dissolution, as illustrated in Fig. 8(b). Fig. 8(c) displays a magnification of this curve. The weight gains due to TiO_2 growth, Al_2O_3 growth, and O dissolution in Ti–6.5Al were 67.7%, 0.6%, and 31.7%, respectively, after 100 h of oxidation. These results are similar to those previously reported for Ti-64 after 100 h of oxidation at 973 K [15]. However, the weight gains due to TiO_2 and Al_2O_3 growth were not measured separately in the previous study. As seen from the results, the weight-gain ratio due to O dissolution relative to the total weight gain in Ti–6.5Al was less than that in pure Ti. This indicates that Al addition and Al_2O_3 formation reduced the TiO_2 growth and O

dissolution rates, particularly affecting the O dissolution rate.

For oxide growth, the simulated temporal changes in the thickness of TiO_2 for pure Ti were in good agreement with the measured data, as illustrated in Fig. 9(a). However, for Ti–6.5Al, the simulated total oxide thickness was smaller than the approximated value (Fig. 9(b)). In addition, the simulated and measured overall weight gains were equivalent to those presented in Fig. 8(b). The simulated total Al_2O_3 thickness in Ti–6.5Al was approximately 18 nm after 45 h, as indicated in Fig. 9(d); therefore, the simulated total thickness in Fig. 9(b) overlapped with that of TiO_2. Notably, the current simulation did not predict the structure of constituent oxides, e.g., a mixture of oxides or oxide layers, because the simulated Al_2O_3 thickness indicated the total thickness of Al_2O_3 per unit area normal to the metal–oxide interface. However, Al_2O_3 may initially form clusters near the gas–oxide interface of the oxide scale, accompanied by the growth of TiO_2 [31]. Al_2O_3 then grows to form a thin layer on the rough TiO_2 surface, which facilitates rough Al_2O_3 surface formation [31,43]. Such external Al_2O_3 formation leads to the formation of thinner TiO_2 (Fig. 9(b)).

The formation of a diffusion barrier in the Al_2O_3 layer hindered O penetration from the surface through the oxide scales. O diffusion in the pure Ti substrate may be similar to that in Ti–6.5Al because this diffusion has been previously observed to be similar for CP-Ti, Ti-64, and Ti–6Al–2Sn–4Zr–2Mo–0.1Si (Ti–6242S) based on their activation energies and preexponential factors [14]. However, the previous study reported a slightly different O diffusion zone depth for Ti-64 and Ti–6242S. Fig. 9(c) presents the temporal changes in the O dissolution depth in pure Ti and Ti–6.5Al in the present study. The O dissolution depth in Ti–6.5Al was approximately 31.4 μm after 45 h of oxidation, which was 4 μm lower than that of pure Ti. This finding indicates that the O diffusion zone in Ti–6.5Al may be thinner than that in pure Ti, as previously reported by Chaze and Coddet [16]. After 5 and 20 h of oxidation, the O diffusion zone depths in Ti–6.5Al were 10.6 and 20.9 μm, respectively. These values are comparable to the measured depths for Ti–6242S after similar times periods [11,14].

In addition, the concentrations of O and Al were simulated for each substrate at various distances from the oxide–metal interface after different oxidation times between 10 and 45 h (Fig. 10). In pure Ti, the O concentration at the oxide–metal interface increased gradually with oxidation time, reaching approximately 30% at 45 h (Fig. 10(a)). In Ti–6.5Al, the O concentration also increased with oxidation time, but was limited to less than 15% after 45 h (Fig. 10(b)). These concentration changes in the substrate are supported by the simulated temporal evolution of the O and Al concentrations at the oxide–metal interface, as illustrated in Fig. 11. This inhibition of O dissolution in Ti–6.5Al resulted in less weight gain than that in pure Ti.

After the oxidation of Ti–6.5Al was initiated, the O concentration rapidly increased from 0.13 at.%, and Al was immediately depleted at the oxide–metal interface. The Al concentration at the oxide–metal interface decreased from 11.02 at.% to approximately 1.4 at.% after 45 h (Fig. 11(b)). However, the Al_2O_3 layer grew continuously from the beginning of the oxidation process, as observed for TiO_2. It should be noted that Al_2O_3 formation alone was unlikely because Al_2O_3 formation and O dissolution without accompanying TiO_2 formation did not achieve the approximated weight gain during oxidation. As illustrated in Fig. 2, an increase in the O concentration at the oxide–metal interface allowed Al_2O_3 to grow despite the small Al concentration at the oxide–metal interface. Furthermore, Al continuously diffused toward the oxide–metal interface from the bulk side during oxidation. Therefore, Al_2O_3 formed even at small Al concentrations by consuming the Al diffused from the bulk substrate. The low Al concentration before oxidation (6.5 wt%) and low Al diffusivity in the substrate constrained the formation of the Al_2O_3 layer, resulting in an Al depletion depth of 0.15 μm from the oxide–metal interface after 45 h (Fig. 10(c)). This simulated depth is considered reasonable based on previously reported STEM measurements for a multicomponent near-α alloy [22].

In contrast, O diffusion in the substrate was faster than Al diffusion. This led to the formation of region with high O and initial Al concentrations in the substrate beneath the Al-depletion zone, although O dissolution was inhibited in Ti–6.5Al compared to that in pure Ti. For example, the Al and O concentrations at a distance of 1 μm from the oxide–metal interface were 11.0 and 13.0 at.%, respectively, after 45 h of oxidation (Fig. 10(b) and (c)). This composition was previously demonstrated to be within the composition range of the α-phase field in the calculated Ti-rich region by superimposing the experimental data [30]. Such an O dissolution zone near the metal–oxide interface has also been observed in the oxidation of other Al-added α- and α–β-Ti alloys

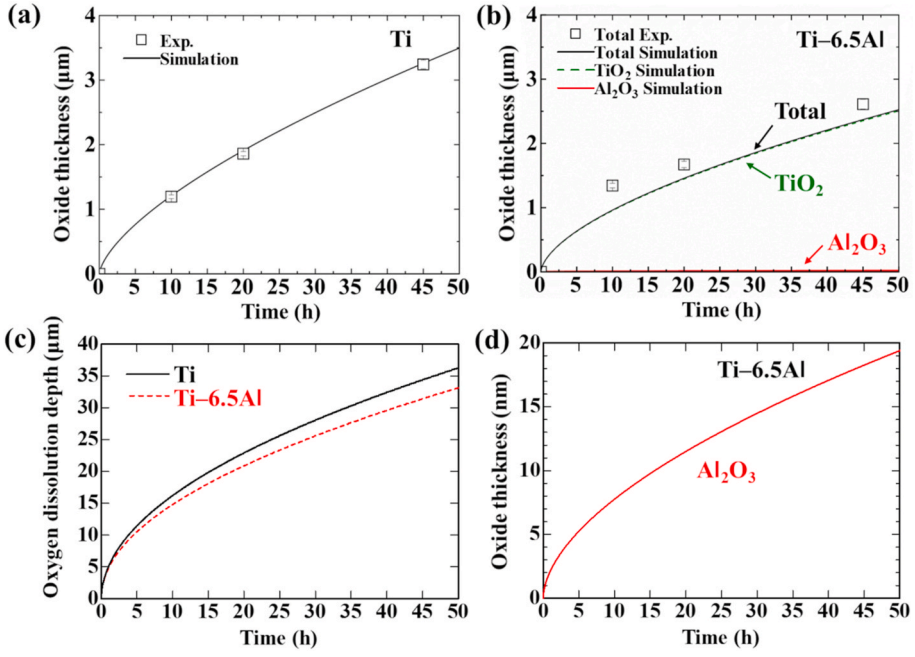

Fig. 9. Measured and simulated total oxide thickness and simulated thickness of TiO_2 and Al_2O_3 oxides for (a) pure Ti and (b) Ti–6.5Al. (c) Simulated temporal changes in the O dissolution depth in pure Ti and Ti–6.5Al. (d) Magnified simulated oxide thickness of Al_2O_3 in Ti–6.5Al, as depicted in (b).

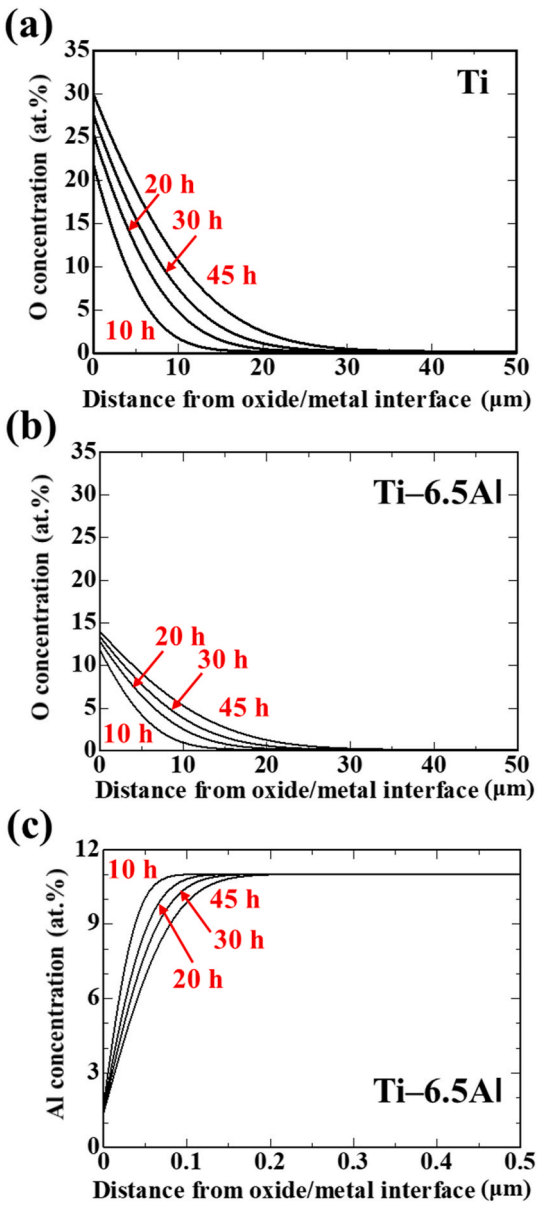

Fig. 10. Simulated O concentration profiles in the substrates of (a) pure Ti and (b) Ti–6.5Al after 10, 20, 30, and 45 h of oxidation. (c) Simulated Al concentration profiles in the Ti–6.5Al substrate after 10, 20, 30, and 45 h of oxidation.

without internal oxidation [4,11,13–16]. In α–β-Ti alloys, the β phase near the metal–oxide interface transforms to the α phase due to O dissolution from the metal surface because O is an α-phase stabilizer. This increase in the Al and O concentrations enhances brittleness near the oxide–metal interface. However, a detailed analysis of the effects of element concentration on surface mechanical properties is left for future research.

The solubility limit of O in α-Ti is dependent on the Al content and temperature of the Ti–Al–O system [30]. This limit decreases with increasing Al concentration and decreasing temperature, where the α_2 phase forms beyond the solubility limit. However, at 973 K, approximately 33 at.% of O can dissolve in α-Ti containing 11 at.% Al [30]. Therefore, in this study, the degree of O dissolution in the substrate was not affected by the decrease in the solubility limit of O due to the addition of Al, but was primarily limited by the diffusion barrier effect of the Al_2O_3 layer.

The simulated and measured total oxide thicknesses exhibited a slight deviation for Ti–6.5Al, as illustrated in Fig. 9(b). This difference

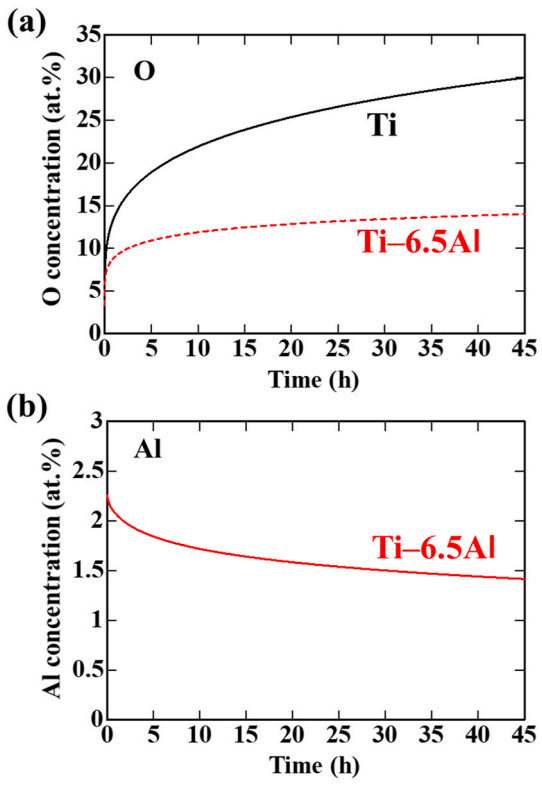

Fig. 11. Simulated temporal changes in (a) O concentration for Ti and Ti–6.5Al and (b) Al concentration for Ti–6.5Al at the metal–oxide interface.

may be attributed to several limitations in the present simulation. These limitations include the use of Al and O diffusivities without nondiagonal components and the determination of oxide formation based on the chemical potentials at the oxide–metal interface, where the activities of oxides were assumed to be 1.

The simulated weight gain and oxide thickness rates were supported by the experimental results. Furthermore, it was demonstrated that Al_2O_3 formation contributed negligibly to the total increase in these parameters with increasing oxidation time. However, Al_2O_3 growth decelerated TiO_2 growth and O dissolution. Future work will aim to improve the models presented in this paper to gain further insight into changes in alloy characteristics with oxidation.

5. Summary and conclusions

This study examined the effect of Al_2O_3 growth at the metal–oxide interface on TiO_2 growth and O dissolution in an Al-added Ti substrate. Weight gain and oxide thickness changes due to Al_2O_3/TiO_2 growth and O dissolution through the substrate during oxidation at 973 K were evaluated in the Al-added Ti–O system using the one-dimensional finite volume method coupled with CALPHAD. Moreover, the temporal evolution of elemental concentrations in the substrate was simulated at the metal–oxide interface. The following insights were obtained from the simulations:

1. The addition of 11.02 at.% Al to the Ti–O system reduced the weight gain due to TiO_2 growth and O dissolution and led to Al_2O_3 growth to a maximum total thickness of approximately 18 nm after 45 h.
2. During the initial stage of oxidation, Al_2O_3 was continuously formed at the metal surface, accompanied by Al depletion and increased O concentration at the oxide–metal interface.
3. O dissolution in the substrate was reduced by Al_2O_3 formation, thereby restricting the increase in the O concentration at the oxide–metal interface.

4. High O diffusivity and low Al diffusivity generated a region with high O and initial Al concentrations beneath the Al-depletion zone in the substrate, which may enhance the surface brittleness.

Funding

This research was supported in part by Amada Foundation (AF-2022215-B3).

Data availability statement

The raw/processed data required to reproduce the above findings cannot be shared at this time, as the data also form part of an ongoing study.

Declaration of competing interest

The authors declare that they have no known competing financial interests or personal relationships that could have appeared to influence the work reported in this paper.

Acknowledgments

The authors are grateful to Mr. Satoshi Iwasaki, Ms. Chiho Togashi, Mr. Koji Nakazato, and Ms. Shinobu Takemura of the National Institute for Materials Science for their experimental assistance.

References

[1] Su Y, Fan H, You FH, Kong F, Wang X, Chen Y. Improved tensile properties of a novel near-α titanium alloy via tailoring microstructure by hot-rolling. Mater Sci Eng A 2020;790:139588. https://doi.org/10.1016/j.msea.2020.139588.
[2] Ma L, Wan M, Li W, Shao J, Bai X, Zhang J. Superplastic deformation mechanical behavior and constitutive modelling of a near-α titanium alloy TNW700 sheet. Mater Sci Eng A 2021;817:141419. https://doi.org/10.1016/j.msea.2021.141419.
[3] Sitnnad M, Spilners A, Katz O. Oxidation of oxygen-saturated titanium. JOM 1955; 7:645–6. https://doi.org/10.1007/BF03377554.
[4] Yang Y, Kitashima T, Hara T, Hara Y, Iwasaki S. Effect of temperature on oxidation behaviour of Ga-containing near-α Ti alloy. Corros Sci 2018;133:61–7. https://doi.org/10.1016/j.corsci.2018.01.018.
[5] Evans RW, Hull RJ, Wilshire B. The effects of alpha-case formation on the creep fracture properties of the high-temperature titanium alloy IMI834. J Mater Process Technol 1996;56:492–501. https://doi.org/10.1016/0924-0136(96)85109-0.
[6] Biallas G, Essert M, Maier HJ. Influence of environment on fatigue mechanisms in high-temperature titanium alloy IMI834. Int J Fatig 2005;27:1485–93. https://doi.org/10.1016/j.ijfatigue.2005.06.009.
[7] Liu F, Chen Y, He C, Li L, Wang C, Li H, Zhang H, Wang Q, Liu Y. Tensile and very high cycle fatigue behaviors of a compressor blade titanium alloy at room and high temperatures. Mater Sci Eng A 2021;811:141049. https://doi.org/10.1016/j.msea.2021.141049.
[8] Stringer J. The oxidation of titanium in oxygen at high temperatures. Acta Metall 1960;8:758–66. https://doi.org/10.1016/0001-6160(60)90170-X.
[9] Unnam J, Shenoy RN, Clark RK. Oxidation of commercial purity titanium. Oxid Met 1986;26:231–52. https://doi.org/10.1007/BF00659186.
[10] Kitashima T, Liu LJ, Murakami H. Numerical analysis of oxygen transport in alpha titanium during isothermal oxidation. J Electrochem Soc 2013;160:C441–4. https://doi.org/10.1149/2.100309jes.
[11] Gaddam R, Sefer B, Pederson R, Antti ML. Oxidation and α-case formation in Ti–6Al–2Sn–4Zr–2Mo alloy. Mater Char 2015;99:166–74. https://doi.org/10.1016/j.matchar.2014.11.023.
[12] Berthaud M, Popa I, Chassagnon R, Heintz O, Lavková J, Chevalier S. Study of titanium alloy Ti6242S oxidation behaviour in air at 560 °C: effect of oxygen dissolution on lattice parameters. Corros Sci 2020;164:108049. https://doi.org/10.1016/j.corsci.2019.06.004.
[13] Vincent B, Optasanu V, Herbst F, Chevalier S, Popa I, Montesin T, Lavisse L. Comparison between the oxidation behaviors of Ti6242S, Ti6246, TiXT alloys, and pure titanium. Oxid Met 2021;96:283–94. https://doi.org/10.1007/s11085-021-10051-w.
[14] Vaché N, Cadoret Y, Dod B, Monceau D. Modeling the oxidation kinetics of titanium alloys: review, method and application to Ti-64 and Ti-6242s alloys. Corros Sci 2021;178:109041. https://doi.org/10.1016/j.corsci.2020.109041.
[15] Frangini S, Mignone A, de Riccardis F. Various aspects of the air oxidation behaviour of a Ti6Al4V alloy at temperatures in the range 600–700 °C. J Mater Sci 1994;29:714–20. https://doi.org/10.1007/BF00445984.
[16] Chaze AM, Coddet C. Influence of alloying elements on the dissolution of oxygen in the metallic phase during the oxidation of titanium alloys. J Mater Sci 1987;22: 1206–14. https://doi.org/10.1007/BF01233110.
[17] Kitashima T, Kawamura T. Prediction of oxidation behavior of near-α titanium alloys. Scripta Mater 2016;124:56–8. https://doi.org/10.1016/j.scriptamat.2016.06.044.
[18] Du HL, Datta PK, Lewis DB, Burnell-Gray JS. Air oxidation behaviour of Ti–6Al–4V alloy between 650 and 850°C. Corros Sci 1994;36:631–42. https://doi.org/10.1016/0010-938X(94)90069-8.
[19] McReynolds KS, Tamirisakandala S. A study on alpha-case depth in Ti-6Al-2Sn-4Zr-2Mo. Metall Mater Trans A 2011;42:1732–6. https://doi.org/10.1007/s11661-011-0710-3.
[20] Leyens C, Peters M, Kaysser WA. Influence of microstructure on oxidation behaviour of near-α titanium alloys. Mater Sci Technol 1996;12:213–8. https://doi.org/10.1179/mst.1996.12.3.213.
[21] Kitashima T, Yamabe-Mitarai Y. Oxidation behavior of germanium- and/or silicon-bearing near-α titanium alloys in air. Metall Mater Trans A 2015;46:2758–67. https://doi.org/10.1007/s11661-015-2835-2.
[22] Kitashima T, Hara T, Yang Y, Hara Y. Oxidation–nitridation-induced recrystallization in a near-α titanium alloy. Mater Des 2018;137:355–60. https://doi.org/10.1016/j.matdes.2017.10.043.
[23] Heuer AH. Oxygen and aluminum diffusion in α-Al2O3: how much do we really understand? J Eur Ceram Soc 2008;28:1495–507. https://doi.org/10.1016/j.jeurceramsoc.2007.12.020.
[24] Bakulin AV, Chumakova LS, Kulkova SE. Study of the diffusion properties of oxygen in TiO_2. J Exp Theor Phys 2021;133:169–74. https://doi.org/10.1134/S1063776121070025.
[25] Uwanyuze RS, Alpay SP, Schafföner S, Sahoo S. A first principles analysis of oxidation in titanium alloys with aluminum and vanadium. Surf Sci 2022;719: 122026. https://doi.org/10.1016/j.susc.2022.122026.
[26] Chaze AM, Coddet C. Influence of aluminium on the oxidation of titanium between 550 and 750 °C. J Less-Common Met 1990;157:55–70. https://doi.org/10.1016/0022-5088(90)90406-A.
[27] Mehrotra S, Kalyan D, Makineni SK, Santra S. Oxide growth characteristics, kinetics and mechanism of rutile formation on pure titanium. Vacuum 2024;219: 112682. https://doi.org/10.1016/j.vacuum.2023.112682.
[28] Köppers M, Herzig C, Friesel M, Mishin Y. Intrinsic self-diffusion and substitutional Al diffusion in α-Ti. Acta Mater 1997;45:4181–91. https://doi.org/10.1016/S1359-6454(97)00078-5.
[29] Barin I. Thermochemical data of pure substances. New York: VCH; 1995.
[30] Lee BJ, Saunders N. Thermodynamic evaluation of the Ti–Al–O ternary system. Z Metallkd 1997;88:152–61.
[31] Valdés-Saucedo OA, Rocha-Moreno RC, Ramírez-Ramírez JH, Pérez-González FA, Colás R, Garza-Montes-de-Oca NF. Characterization of the high temperature isothermal oxidation behaviour of an ATI425® titanium alloy. Oxid Met 2021;95: 427–44. https://doi.org/10.1007/s11085-021-10032-z.
[32] Nijdam TJ, Jeurgens LPH, Sloof WG. Promoting exclusive α-Al2O3 growth upon high-temperature oxidation of NiCrAl alloys: experiment versus model predictions. Acta Mater 2005;53:1643–53. https://doi.org/10.1016/j.actamat.2004.12.014.
[33] Nijdam TJ, Jeurgens LPH, Sloof WG. Modelling the thermal oxidation of ternary alloys—compositional changes in the alloy and the development of oxide phases. Acta Mater 2003;51:5295–307. https://doi.org/10.1016/S1359-6454(03)00381-1.
[34] Lavisse L, Berger P, Kanjer A, Optasanu V, Gorny C, Peyre P, François M, Montesin T, Marco de Lucas MC. Tracking the role of nitrogen in the improvement of the high temperature oxidation resistance of titanium by mechanical treatments. Corros Sci 2022;197:110080. https://doi.org/10.1016/j.corsci.2021.110080.
[35] Chou K, Chu PW, Levi CG, Marquis EA. Influence of a silicon-bearing film on the early stage oxidation of pure titanium. J Mater Sci 2017;52:9884–94. https://doi.org/10.1007/s10853-017-1143-1.
[36] Kofstad P, Anderson PB, Krudtaa OJ. Oxidation of titanium in the temperature range 800–1200°C. J Less Common Met 1961;3:89–97. https://doi.org/10.1016/0022-5088(61)90001-7.
[37] Lopes Gomes JE, Huntz AM. Correlation between the oxidation mechanism of titanium under a pure oxygen atmosphere, morphology of the oxide scale, and diffusional phenomena. Oxid Met 1980;14:249–61. https://doi.org/10.1007/bf00604567.
[38] Kofstad P, Hauffe K, Kjöllesdal H. Investigation of the oxidation mechanism of titanium. Acta Chem Scand 1958;12:239–66. https://doi.org/10.3891/acta.chem.scand.12-0239.
[39] Chen W, Li Q, Zhou L, Qiu W, Ren Y, Li C, Chen J, Lin Y, Zhou K. Oxidation mechanism of a near β-Ti alloy. Mater Des 2022;223:111144. https://doi.org/10.1016/j.matdes.2022.111144.
[40] Brumm MW, Grabke HJ. The oxidation behaviour of NiAl-I. Phase transformations in the alumina scale during oxidation of NiAl and NiAl-Cr alloys. Corros Sci 1992; 33:1677–90. https://doi.org/10.1016/0010-938X(92)90002-K.
[41] Levin I, Brandon D. Metastable alumina polymorphs: crystal structures and transition sequences. J Am Ceram Soc 1998;81:1995–2012. https://doi.org/10.1111/j.1151-2916.1998.tb02581.x.
[42] Lu W, Chen CL, He LL, Wang FH, Lin JP, Chen GL. (S)TEM study of different stages of Ti–45Al–8Nb–0.2W–0.2B–0.02Y alloy oxidation at 900 °C. Corros Sci 2008;50: 978–88. https://doi.org/10.1016/j.corsci.2007.11.013.
[43] Dong E, Yu W, Cai Q, Cheng L, Shi J. High-temperature oxidation kinetics and behavior of Ti–6Al–4V alloy. Oxid Met 2017;88:719–32. https://doi.org/10.1007/s11085-017-9770-0.